Supporting Information

Excitation Energy Delocalization and Transfer to Guests within $M^{II}_4L_6$ Cage Frameworks

Andrew J. Musser,[†,‡,⊥] Prakash P. Neelakandan,[§,⊥,∥] Johannes M. Richter,[†] Hirotaka Mori,[§,#] Richard H. Friend,[*,†] and Jonathan R. Nitschke[*,§]

Contents

S1. General experimental techniques

All reagents and solvents were purchased from commercial sources and used as supplied. All experiments were carried out at room temperature unless otherwise stated. NMR spectra were recorded using either a Bruker DRX-400, a Bruker AVC-500-BB or a Bruker AVC-500-TCI spectrometer. Chemical shifts of cages are reported in parts per million (δ) calibrated to the residual solvent signals: δH with acetonitrile-d_3 at 1.940 ppm and δC with acetonitrile-d_3 at 118.260 ppm. High resolution mass spectrometry was performed on a Waters LCT Premier Mass Spectrometer featuring a Z-spray source with electrospray ionization and modular LockSpray interface. Molecular modelling was done using the modified MM2 force field of CAChe Workspace, WorkSystem Pro Version 7.5.0.85. UV-Vis absorption measurements were performed on a Perkin-Elmer Lambda 750 spectrometer.

S2. Syntheses

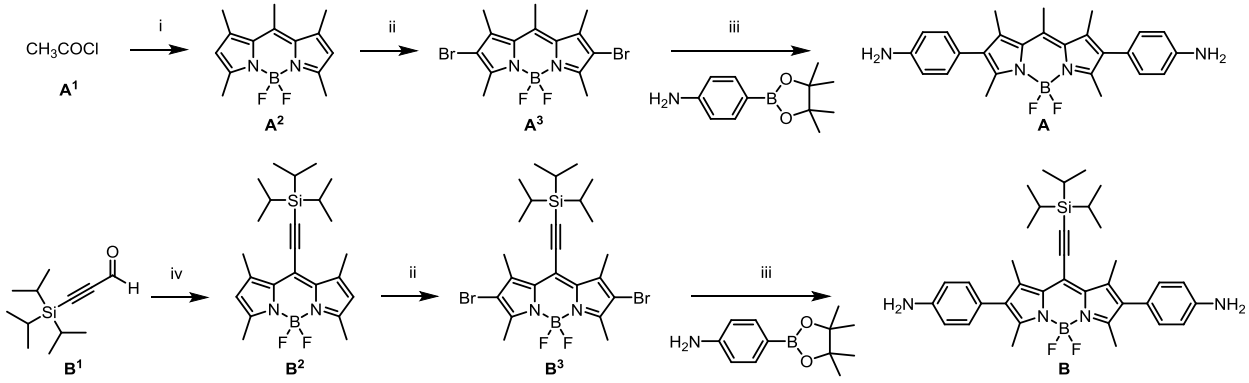

(i) (a) 2,4-Dimethylpyrrole (2.0 eq), CH_2Cl_2, reflux, 1 h, (b) NEt_3 (3 eq), $BF_3{\cdot}OEt_2$ (4.5 eq), CH_2Cl_2, rt, 10 min. (ii) N-Bromosuccinimide (3.5 eq), CH_2Cl_2, r.t., 1 h. (iii) $Pd(dppf)Cl_2{\cdot}CH_2Cl_2$ (20 mol%), K_2CO_3 (6.0 eq), 1,4-dioxane/H_2O (3:1), reflux (110 °C), 90 min. (iv) (a) 2,4-Dimethylpyrrole (2.0 eq), trifluoroacetic acid (5 mol%), CH_2Cl_2, 0 °C, 1 h, (b) 2,3-dichloro-5,6-dicyano-1,4-benzoquinone (1.0 eq), 5 min., (c) NEt_3 (6.0 eq), $BF_3{\cdot}OEt_2$ (8.0 eq), 5 min. (TFA = trifluoroacetic acid, DCM = dichloromethane, DDQ = 2,3-dichloro-5,6-dicyano-p-benzoquinone, NBS = N-bromosuccinimide, dppf = 1,1'-bis(diphenylphosphino)ferrocene).

Scheme S1. Synthesis of BODIPY ligands **A** and **B**.

S2.1. Synthesis of A

A² and **A³** were synthesized as reported elsewhere.[1] **A³** (210 mg, 0.50 mmol), [1,1'-bis(diphenylphosphino)ferrocene]dichloropalladium(II) complex with dichloromethane (82 mg, 20 mol%), potassium carbonate (415 mg, 6.0 eq.), and 4-aminophenylboronic acid pinacol ester (438 mg, 4.0 eq.) were added to a Schlenck flask, and the flask was filled with nitrogen by using the standard Schlenck technique. After addition of 1,4-dioxane (7.5 mL) and water (2.5 mL) at room temperature, the mixture was heated at reflux for 90 m. After cooling the reaction mixture to room temperature, AcOEt (20 mL) was added to quench the reaction. The mixture was dried over magnesium sulfate and passed through a short silica column with DCM/AcOEt. After removing the solvent in vacuo, the resulting residue was purified by silica gel column chromatography with a mixture of DCM, *n*-hexane and AcOEt (8:1:1) followed by recrystallization from DCM/*n*-hexane to yield **A** as green solid (138 mg, 62% yield). ^{1}H NMR (400 MHz, CD_3CN, 300 K): δ (ppm) 6.98 (dt, 4H, J_1 = 6.8 Hz, J_2 = 2.0 Hz), 6.73 (dt, 4H, J_1 = 6.8 Hz, J_2 = 2.0 Hz), 4.24 (br s, 4H), 2.75 (s, 3H), 2.39 (s, 6H), and 2.34 (s, 6H); ^{13}C NMR (400 MHz, CD_3CN, 300 K): δ (ppm) 13.48, 15.65, 17.82, 115.20, 122.34, 131.98, 132.82, 134.59,

138.25, 143.80, 148.18, and 152.71; ^{19}F NMR (400 MHz, CD_3CN, 300 K): δ (ppm) –145.16 (q, 2F, J = 17.2 Hz); HRMS (ESI): *m/z* calculated for $C_{26}H_{28}BF_2N_4$ [*M*–H]$^+$: 445.3448, found: 445.3433.

S2.2. Synthesis of B^2

To a solution of 3-(triisopropylsilyl)-1-propynal (**B^1**, 1.10 g, 5.23 mmol) and 2,4-dimethylpyrrole (1.08 mL; 2.0 eq.) in dry DCM (20 mL) was added trifluoroacetic acid (20 μL, 5 mol%), and the resulting solution was stirred under N_2 atmosphere at 0 °C for 1 h. After addition of 2,3-dichloro-5,6-dicyanobenzoquinone (DDQ, 1.19 g, 1.0 eq.), the solution was stirred for 5 m and then triethylamine (4.37 mL, 6.0 eq) and $BF_3{\cdot}OEt_2$ (5.16 mL; 8.0 eq.) were added. After further 5 m, the resulting solution was passed through a short alumina column with DCM to remove tar and residual DDQ. The reaction mixture was purified by silica-gel chromatography using a mixture of 50% DCM and *n*-hexane as eluent followed by recrystallization from DCM/MeOH to give **B^2** as green crystals (1.02 g, 46% yield). ^{1}H NMR (400 MHz, $CDCl_3$, 300 K): δ (ppm) 6.04 (s, 2H), 2.51 (s, 6H), 2.47 (s, 6H), and 1.14 (m, 21H); ^{13}C NMR (400 MHz, $CDCl_3$, 300 K): δ (ppm) 11.43, 14.62, 15.82, 18.59, 101.70, 112.91, 120.74, 133.28, 142.24, and 154.37; ^{19}F NMR (400 MHz, $CDCl_3$, 300 K): δ (ppm) –146.33 (q, 2F, J = 17.2 Hz).

S2.3. Synthesis of B^3

To a solution of **B^2** (86 mg, 0.20 mmol) in dry DCM (10 mL) was added *N*-bromosuccinimide (125 mg, 3.5 eq.), and the resulting solution was stirred under N_2 atmosphere at ambient temperature for 1 h. After addition of dry acetone (1.0 mL), the solvent was removed in vacuo. The reaction mixture was purified by silica gel chromatography (DCM:*n*-hexane = 3:1) followed by recrystallization from DCM/MeOH to give **B^3** as green crystals (104 mg, 88% yield). ^{1}H NMR (400 MHz, $CDCl_3$, 300 K): δ (ppm) 2.56 (s, 6H), 2.51 (s, 6H), and 1.15 (m, 21H); ^{13}C NMR (400 MHz, $CDCl_3$, 300 K): δ (ppm) 11.40, 13.66, 14.97, 18.59, 101.51, 111.39, 115.96, 121.02, 132.17, 139.66, and 152.67; ^{19}F NMR (400 MHz, $CDCl_3$, 300 K): δ (ppm) –146.07 (q, 2F, J = 17.2 Hz).

S2.4. Synthesis of B

B^3 (117 mg, 0.20 mmol), [1,1'-bis(diphenylphosphino)ferrocene]dichloropalladium(II) complex with dichloromethane (33 mg, 20 mol%), potassium carbonate (166 mg, 6.0 eq.), and 4-aminophenylboronic acid pinacol ester (175 mg, 4.0 eq.) were added to a Schlenck flask, and the flask was filled with nitrogen by using the standard Schlenck technique. After addition of 1,4-dioxane (3.0 mL) and water (1.0 mL) at room temperature, the mixture was heated at reflux for 90 m. After cooling the reaction mixture to room temperature, ethylacetate (20 mL) was added to quench the reaction. The mixture was dried over magnesium sulfate and passed through a short silica column with DCM/AcOEt. After removing the solvent in vacuo, the resulting residue was purified by silica gel column chromatography with a mixture of DCM, *n*-hexane and AcOEt (5:5:1) followed by recrystallization from DCM/*n*-hexane to yield **A** as a green solid (77 mg, 63% yield). ^{1}H NMR (400 MHz, CD_3CN, 300 K): δ (ppm) 7.00 (dt, 4H, J_1 = 6.8 Hz, J_2 = 2.0 Hz), 6.72 (dt, 4H, J_1 = 6.8 Hz, J_2 = 2.0 Hz), 4.25 (br s, 4H), 2.45 (s, 6H), and 2.42 (s, 6H); ^{13}C NMR (400 MHz, CD_3CN, 300 K): δ (ppm) 12.12, 13.67, 14.68, 18.87, 102.90, 115. 10, 115.18, 120.90, 122.30, 131.79, 133.80, 134.70, 138.81, 148.31, and 154.12; ^{19}F NMR (400 MHz, CD_3CN, 300 K): δ (ppm) –144.71 (q, 2F, J = 17.2 Hz); HRMS (ESI): *m/z* calculated for $C_{36}H_{46}BF_2N_4Si$ [*M*–H]$^+$: 611.6838, found: 611.6852.

S2.5. Procedure for the preparation of cages

In a Schlenk flask, ligand (1 eq.), 2-formylpyridine (2 eq.) and the divalent metal salt (0.67 eq.) were dissolved in acetonitrile (3 mL). The solution was degassed by three evacuation/nitrogen-fill cycles and heated to 70 °C overnight. After cooling to room temperature, the solvent was evaporated off and any unreacted starting materials were removed by trituration with diethyl ether to yield the cages in >95% yield.

S3. Characterization of empty cages

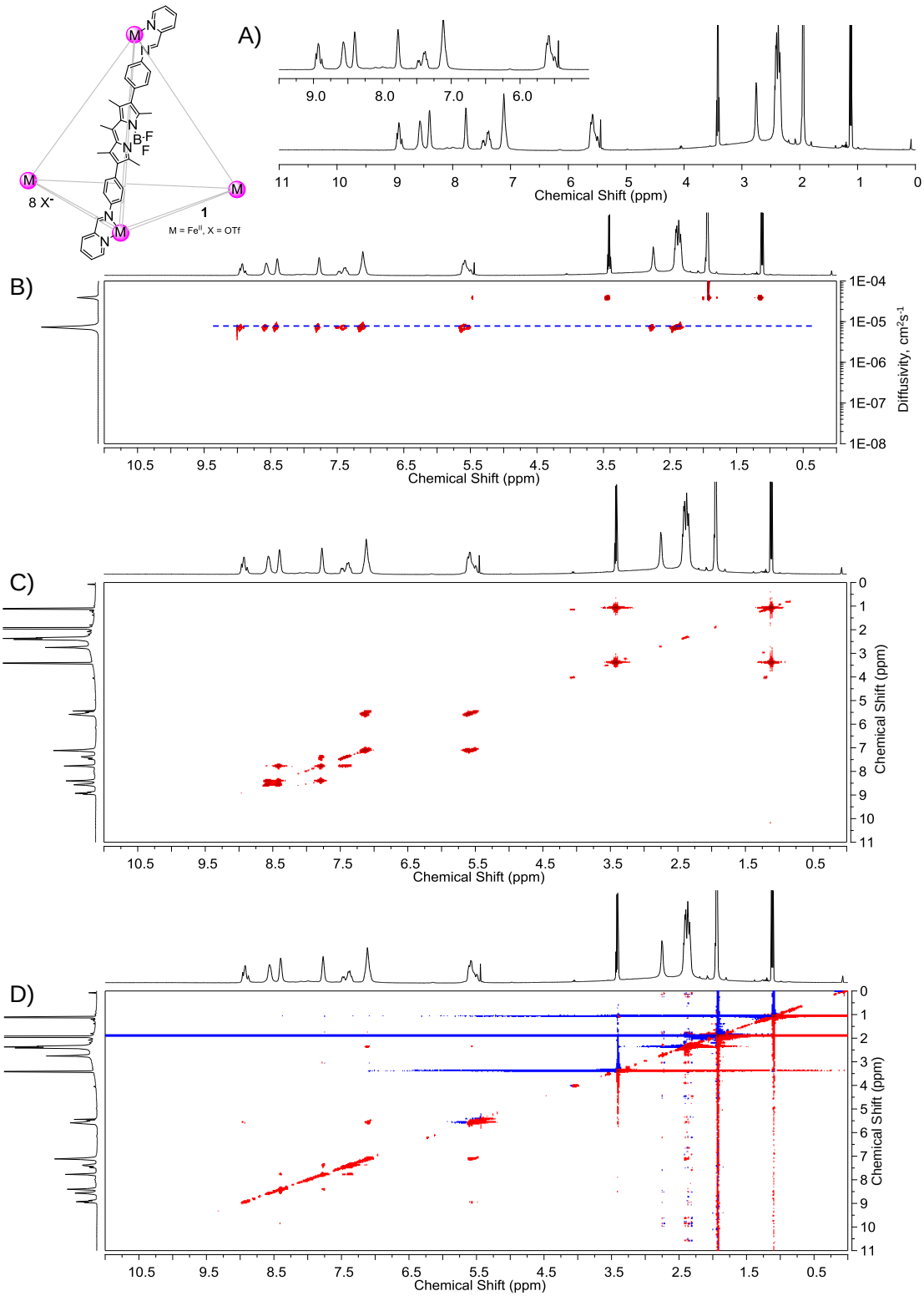

Figure S1. (A) ^{1}H NMR, (B) DOSY, (C) COSY and (D) NOESY spectra of cage **1** in CD_3CN.

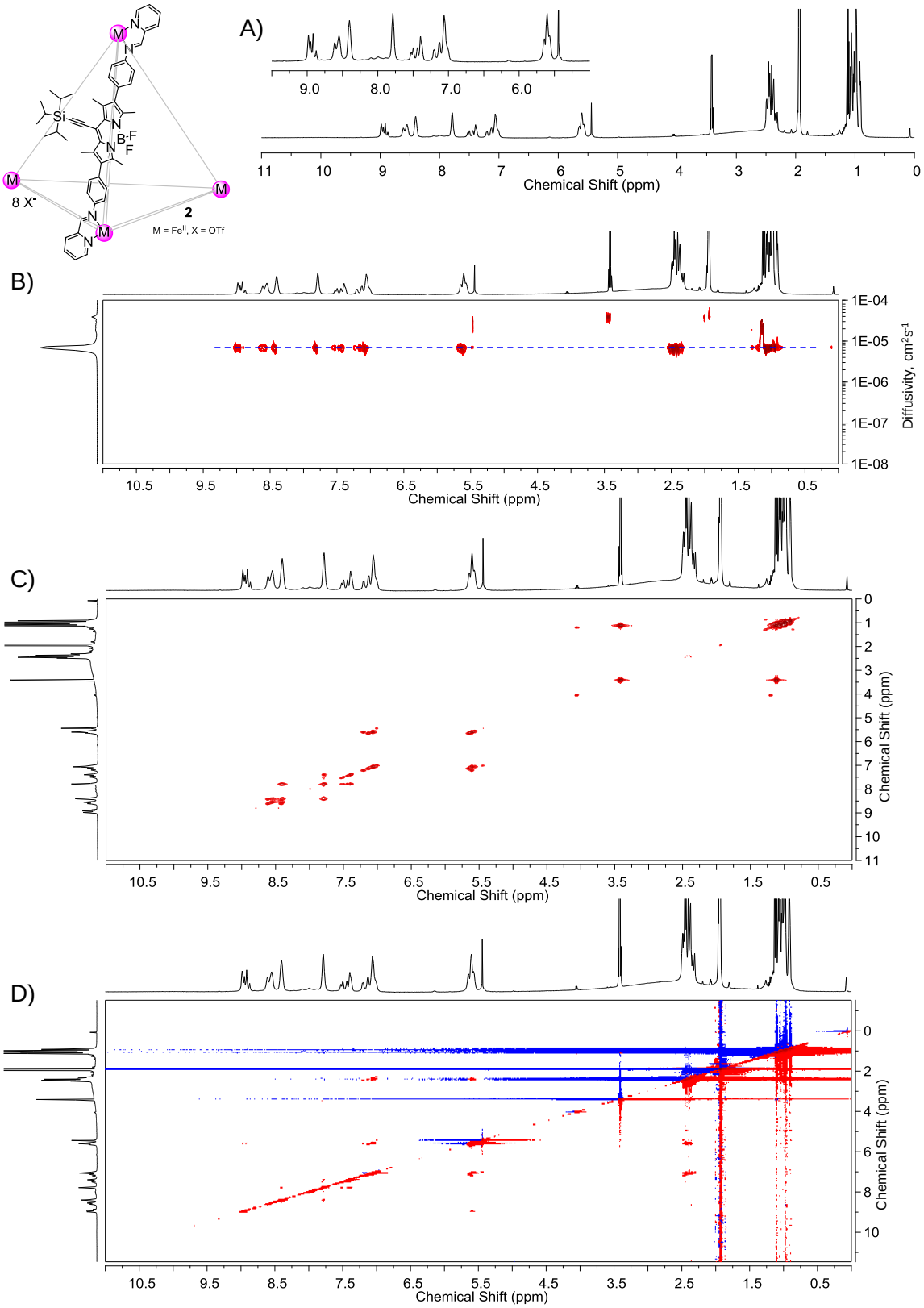

Figure S2. (A) ^{1}H NMR, (B) DOSY, (C) COSY and (D) NOESY spectra of cage **2** in CD_3CN.

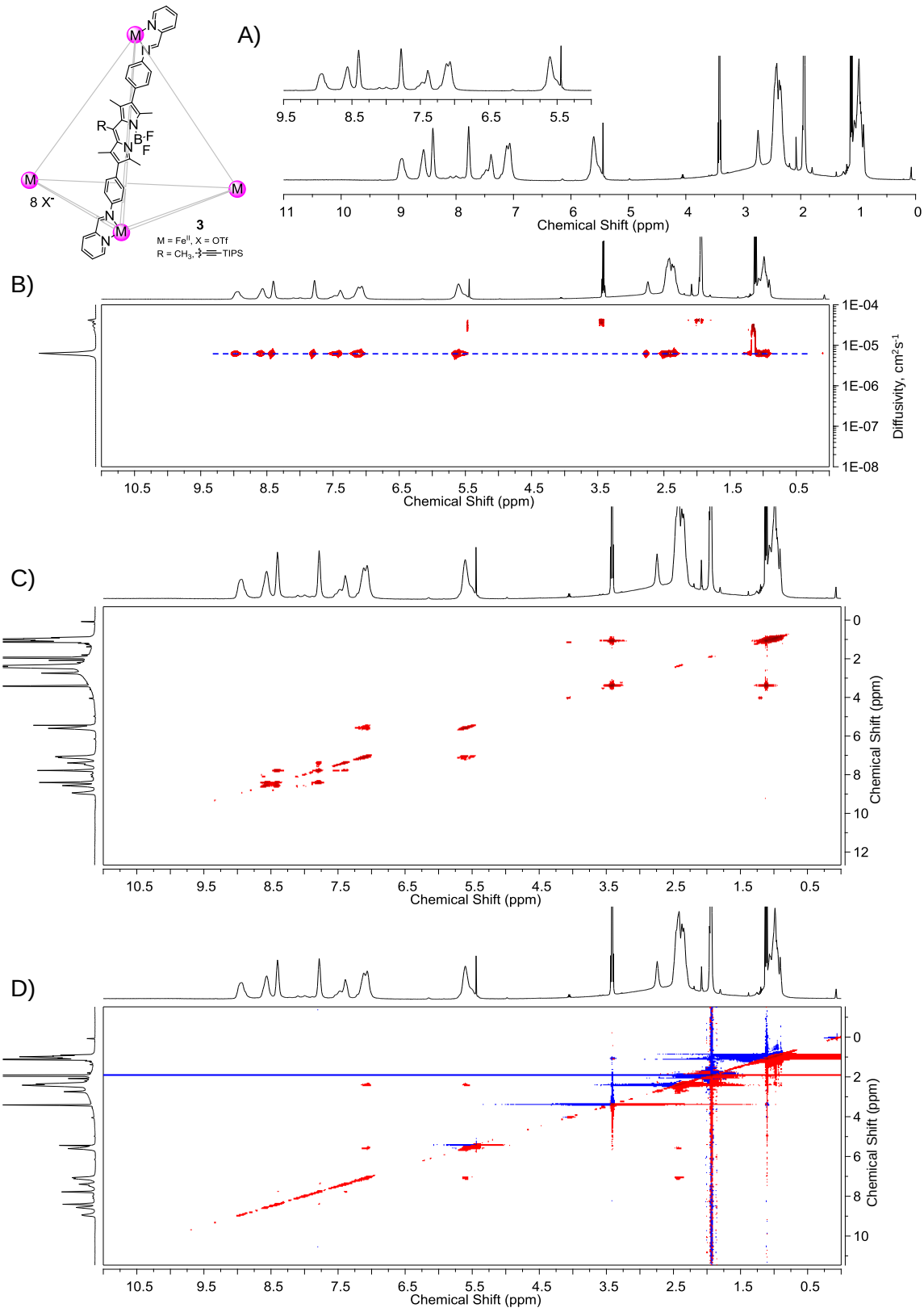

Figure S3. (A) ^{1}H NMR, (B) DOSY, (C) COSY and (D) NOESY spectra of collection of cages **3** in CD_3CN.

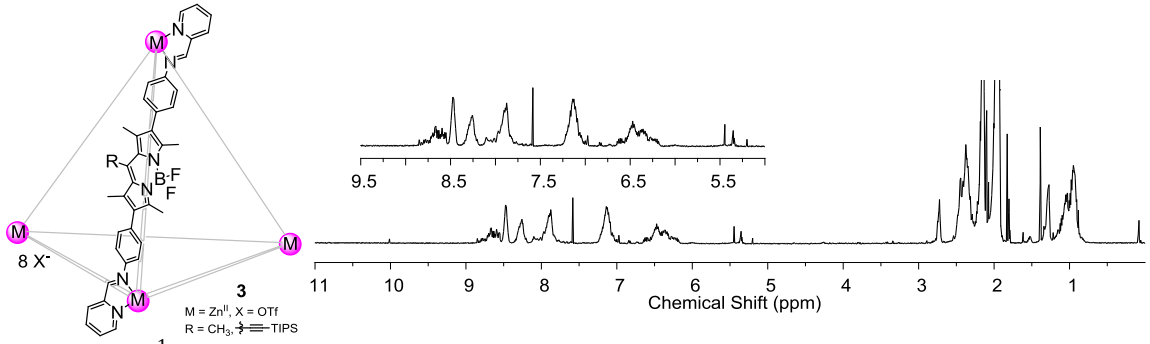

Figure S4. (A) ^{1}H NMR spectrum of collection of cages **4** in CD_3CN.

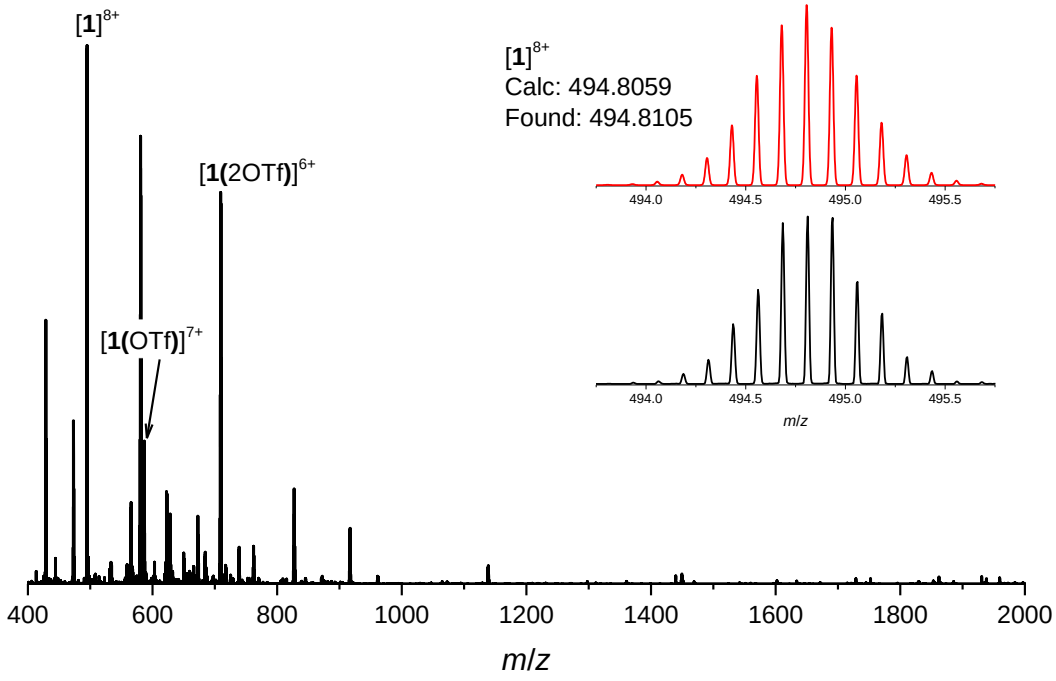

Figure S5. High-resolution mass spectrum of cage **1**. Inset shows the simulated (red) and experimental (black) isotopic distributions of $[\mathbf{1}]^{8+}$.

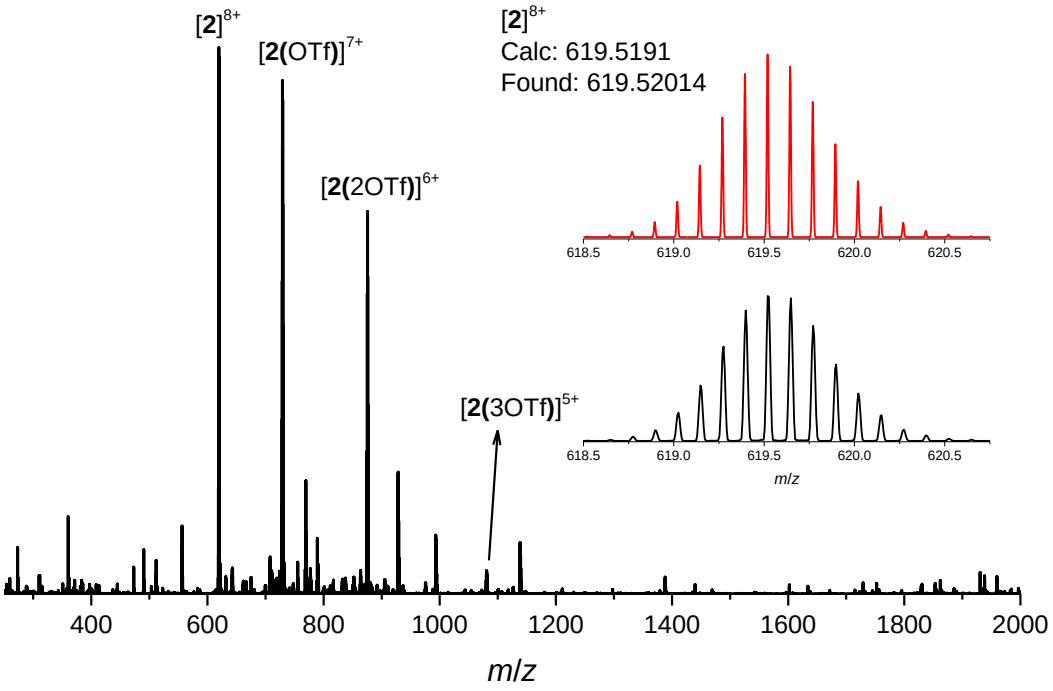

Figure S6. High-resolution mass spectrum of cage **2**. Inset shows the simulated (red) and experimental (black) isotopic distributions of $[\mathbf{2}]^{8+}$.

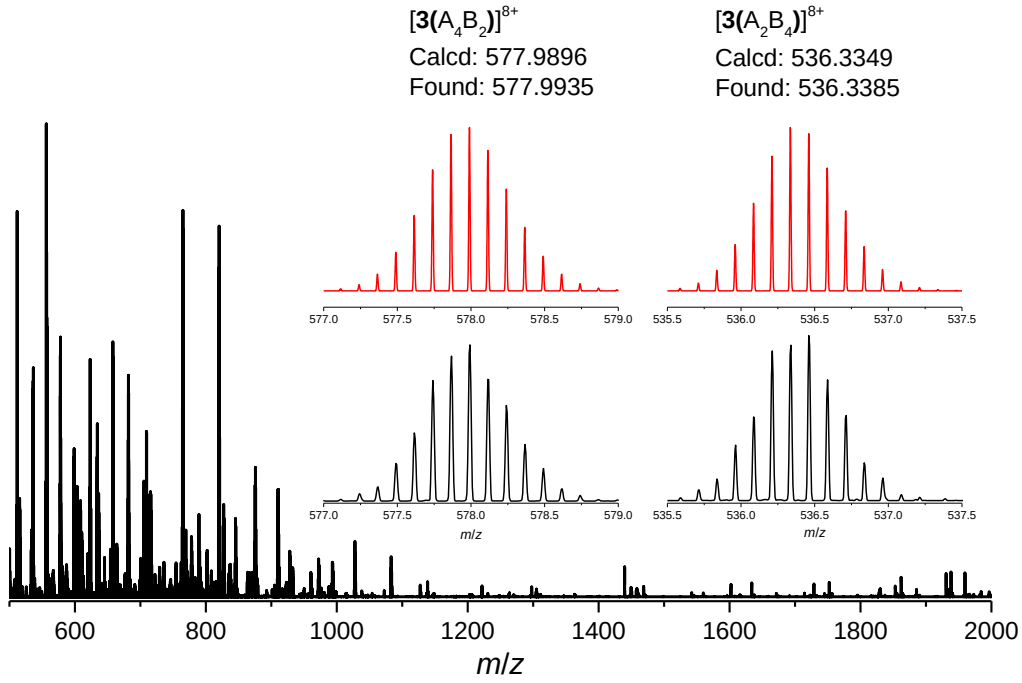

Figure S7. High-resolution mass spectrum of collection of cages **3**. Inset shows the simulated (red) and experimental (black) isotopic distributions for two constitutionally distinct cages.

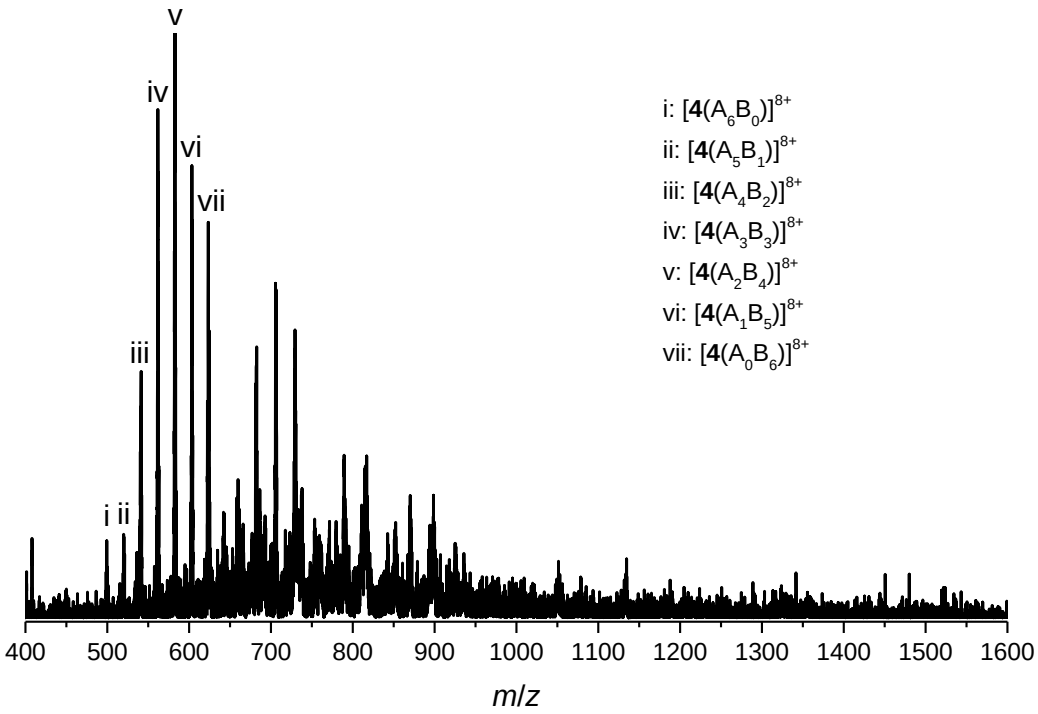

Figure S8. Mass spectrum of collection of cages **4**.

S4. Comparison of PMMA films and CH_3CN solutions

To ensure the PMMA films studied in this report are representative of isolated cages and thus afford insight into intra-cage photophysics, we also prepared dilute solutions of cages **1**-**3**. For these measurements, fresh 1 mg/mL stock solutions were diluted ~1000× to achieve an optical density of 0.1-0.3 in a 1 mm path-length cuvette. The UV-Vis absorption spectrum was immediately taken, and is presented in Figure S9. It was observed that over the course of several hours in the dark, and even faster under laser exposure, the absorption lineshapes of the solvated cages changed and PL quantum yields increased, yielding spectra characteristic of isolated cage components. The similarity of spectral shape between fresh solutions and PMMA films confirms that the cages are not aggregated into higher-order structures in our samples. The slight red-shift evident throughout the spectrum in PMMA-embedded cages is due to increased dispersive interactions in the solid state. Figure S9 also presents the absorption spectrum of Zn^{II}-based heteroleptic cage **4**, which is almost identical in the primary BODIPY absorption region (>450 nm) to Fe^{II}-based **3**. **4** exhibits very slightly reduced absorption strength in the band ~515 nm relative to the band at ~575 nm, but it is nonetheless evident that the type of metal ion at the vertices exerts little influence on the interaction between BODIPY edges in the ground state.

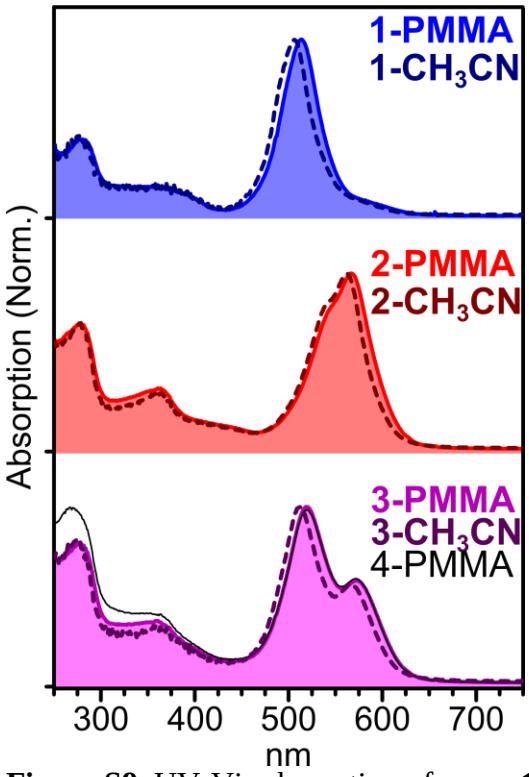

Figure S9. UV-Vis absorption of cages **1**-**3** embedded in PMMA film (thick lines, filled) with corresponding freshly diluted solutions in CH_3CN (dashed). Absorption spectrum of Zn^{II}-based heteroleptic cage **4** (thin black) also included for reference.

S5. Diamine ligand photophysics

For solution measurements, diamines **A** and **B** were dissolved in CH_3CN to give a peak optical density at the absorption maximum in the visible of ~0.3 in a 1 mm cuvette. Immobilized diamine in PMMA matrix were prepared following the same protocol as for cages. Excitation of **A** in solution (Figure S10a) initially yields a broad stimulated emission (SE) band in the visible range, 600-700 nm. This feature rapidly decays, concomitant with a growth of a new positive (i.e. SE) band in the NIR, 800-950 nm. Such a low-energy emissive state must be a charge transfer state, and the ability to resolve it in SE reveals that it has non-zero oscillator strength connecting it to the ground state, i.e. the ground state must have some degree of charge-transfer character. The lifetime of this state is very short, with complete ground-state recovery by ~100 ps (Figure S10c). The charge-transfer process is completely suppressed in PMMA matrix (Figure S10b), affording a much longer excited-state lifetime (Figure S10c). Very similar effects are observed in solutions and films of **B** (Figure S10d-f), with faster time constants for each stage of the progression.

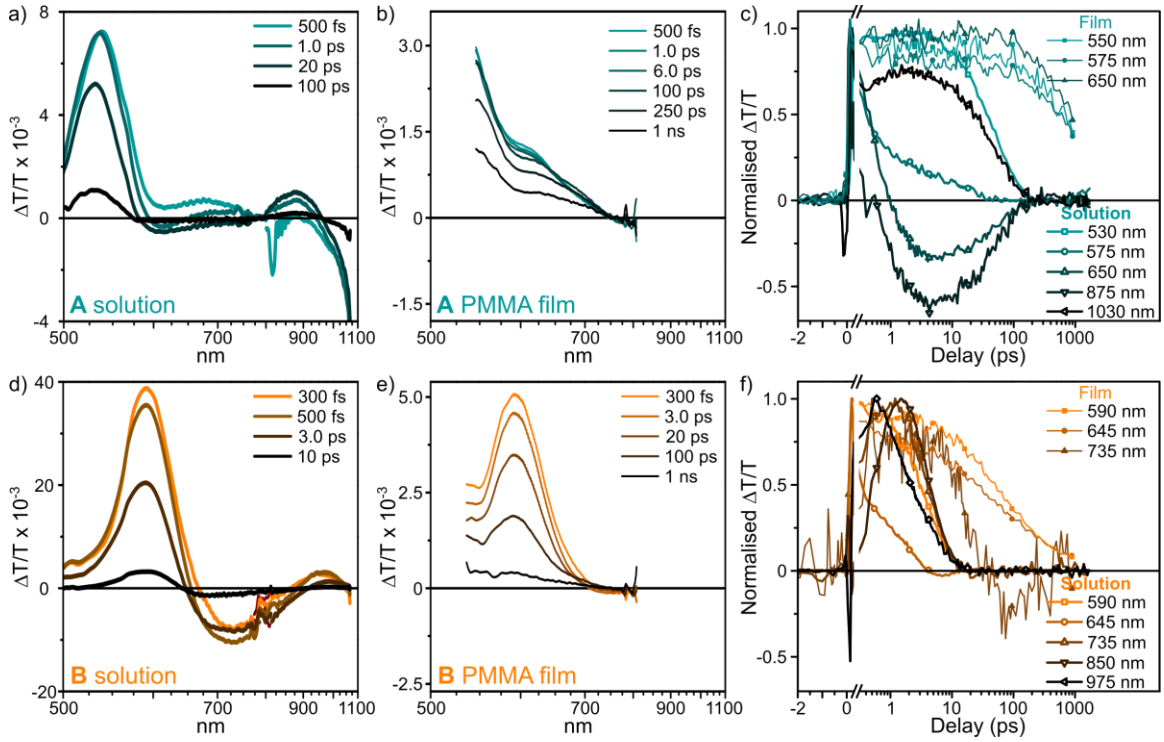

Figure S10. TA spectroscopy of diamine ligands. TA spectra of **A** in (a) CH_3CN solution and (b) PMMA matrix, as well as (c) integrated decay kinetics, reveal charge transfer in solution which is suppressed in film. Similar measurements on (d) solutions and (e) PMMA films of **B** and (f) the corresponding kinetics reveal the same processes. Excitation was at 530 nm.

S6. BODIPY cage transition dipole moments

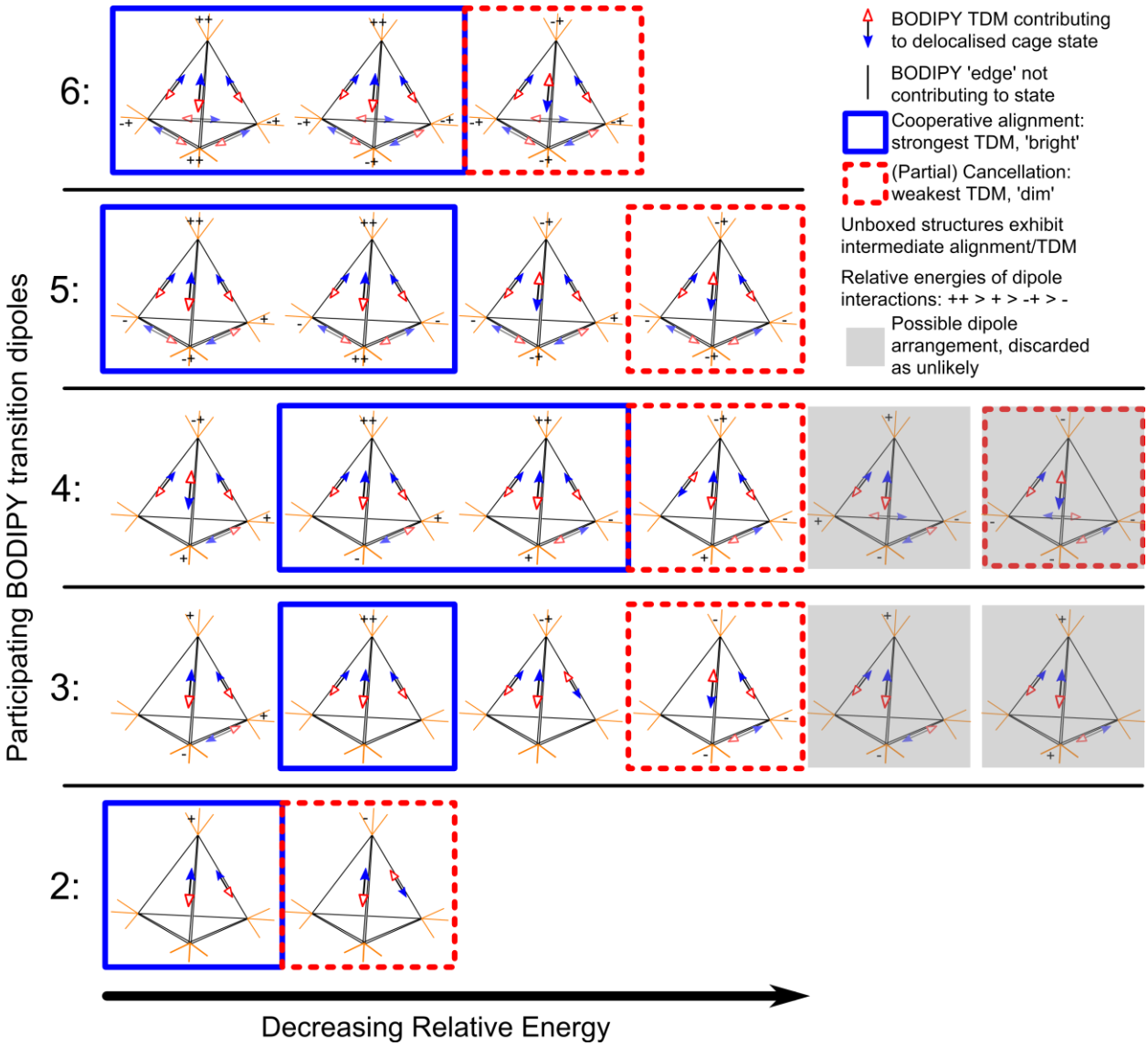

Figure S11. Possible BODIPY transition dipole configurations for dipole-dipole-coupled states, grouped by the number of participating BODIPY molecules. Only symmetry-distinct configurations are shown. Greyed-out structures are possible but considered unlikely due to the larger average distances between chromophores. Regardless of the number of participating molecules, the brightest states (blue boxes) tend to have highest energy, while the states with most cancellation of transition dipole moment (red dashed) have lowest energy. This analysis assumes that the BODIPY transition dipole moment is parallel to the cage edge, which is not strictly true – the slight angle it forms with the edge and its freedom to rotate introduces additional channels for constructive or destructive alignment of transition dipoles and mechanisms of interconversion. Likewise, the BODIPY transition dipoles in cages **2** have significant 'off edge' components due to the conjugation of the TIPS group.

S7. Steady-state photoluminescence

Films of **1-4** (empty and fullerene-loaded) embedded in PMMA were excited at 407 nm. Very weak steady-state PL could be detected, with good spectral agreement with the transient-grating PL measurements presented in the main text. Little change was observed upon encapsulation of C_{60}, but in the presence of C_{70} a new emissive band can be detected >650 nm. This is a useful secondary confirmation of the presence of C_{70} in the cages. The overall PL quantum efficiency in all samples was of order 10^{-4}, below the threshold for precise determination on our system.

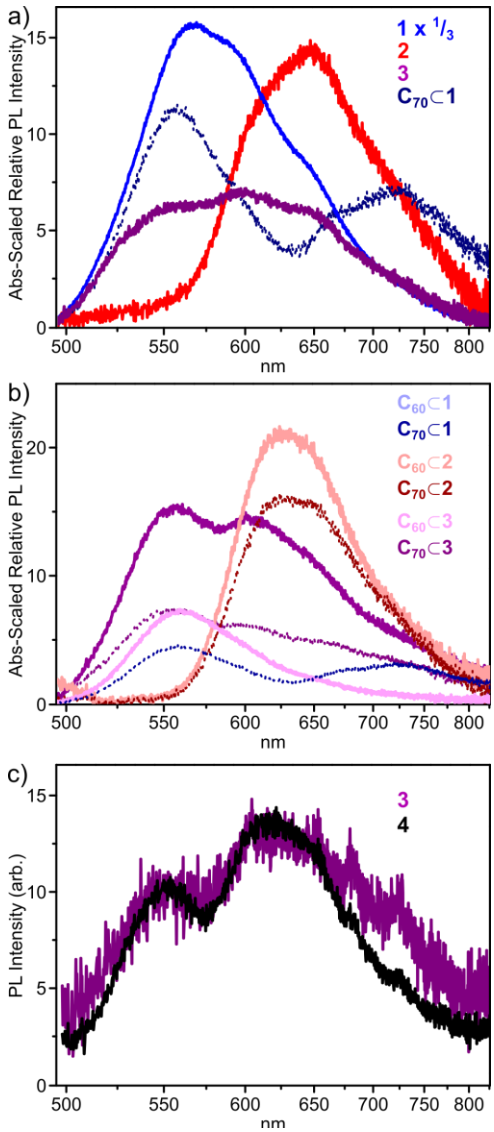

Figure S12. Steady-state PL of **1-3** embedded in PMMA matrices, both (a) without and (b) with encapsulated fullerenes. Data were scaled to account for relative absorption strength at the excitation wavelength (407 nm), to enable comparison of relative PL quantum efficiency. The film C_{70}⊂**1** in panels (a) and (b) is the same, though the arbitrary scale is different. (c) Steady-state PL of **3** and **4** are nearly identical, and importantly exhibit the same relative weights of emission in the regions characteristic of **1** and **2**, suggesting similar compositions and excited-state photophysics. Spectra are scaled to match in intensity.

S8. Empty cage excitation wavelength dependence

Full TA measurements were performed on **1**-**4** at excitation wavelengths of 515 nm, 540 nm and 575 nm. **1** was also excited at 625 nm over a much more limited temporal range (due to low signal), to fully demonstrate the possibility of directly exciting the dim aggregate species II.**1** exhibits strong excitation wavelength dependence in its TA spectra and dynamics (Figure S15), due to the spectral separation of excitonic and CT absorption bands depicted in main-text Figure 3. As the excitation is moved to longer wavelengths (lower energies), the initial GSB peak at 515 nm becomes progressively weaker relative to the band at 580 nm. Likewise, the initial fast decay channel (I→II conversion) makes a progressively smaller contribution to the kinetics, as more II is directly photoexcited. By contrast, there is relatively little change in **2** through the excitation wavelength series (Figure S13), possibly because the off-axis transition dipole moment contribution from the TIPS groups alters the coupling rules of bright/dark states. There is evidence for internal conversion into a similar low-energy dark state in **2**, but this state has no absorption cross-section detectable above the main bright bands. The progression of states I→II→III is largely unchanged with excitation energy, and each conversion is slightly slower than in **1**. Heteroleptic cages **3** exhibit a hybrid of this behaviour (Figure S14), though as discussed in the main text the data cannot be reconstructed from results on homoleptic **1** and **2**. Changes in spectral shape notwithstanding, the underlying dynamics in **3** are little affected by excitation wavelength, suggesting that whatever subset of cages the excitation selects (more **1**-like or **2**-like), the same processes occur. Very similar results are also obtained for heteroleptic **4** (Figure S16), in which the Fe ions at the vertices are replaced with Zn. The direct spectral comparison with **3** reveals that **1**-selective excitation (515 nm) results in a larger relative **1**-type signal in **4**, and likewise **2**-selective excitation (575 nm) results in a larger relative **2**-type signal than in **3**. We stress that the 'unselected' signals (i.e. **2**-type following excitation at 515 nm) are still stronger than would be expected for a mixed population of homoleptic cages. This result indicates that the electronic coupling that mediates delocalization is somewhat weakened in **4** due to the change in through-bond interactions between BODIPY chromophores. Nonetheless, it still remains strong enough to give some evidence of delocalization following the logic of main-text Figure 4.

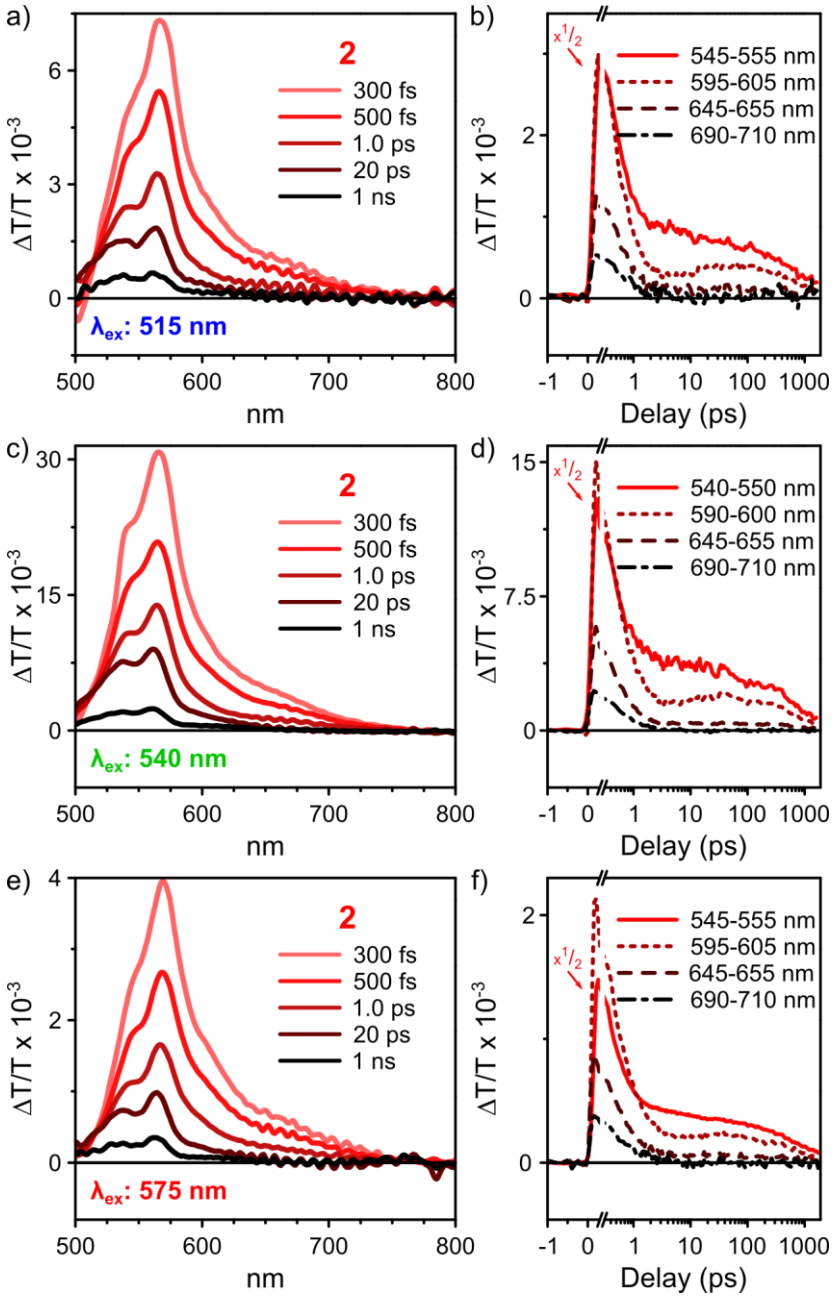

Figure S13. TA excitation dependence of **2**. Spectra (left) and corresponding integrated decay kinetics (right) following excitation at (a, b) 515 nm, (c, d) 540 nm and (e, f) 575 nm. No significant changes are observed through the series.

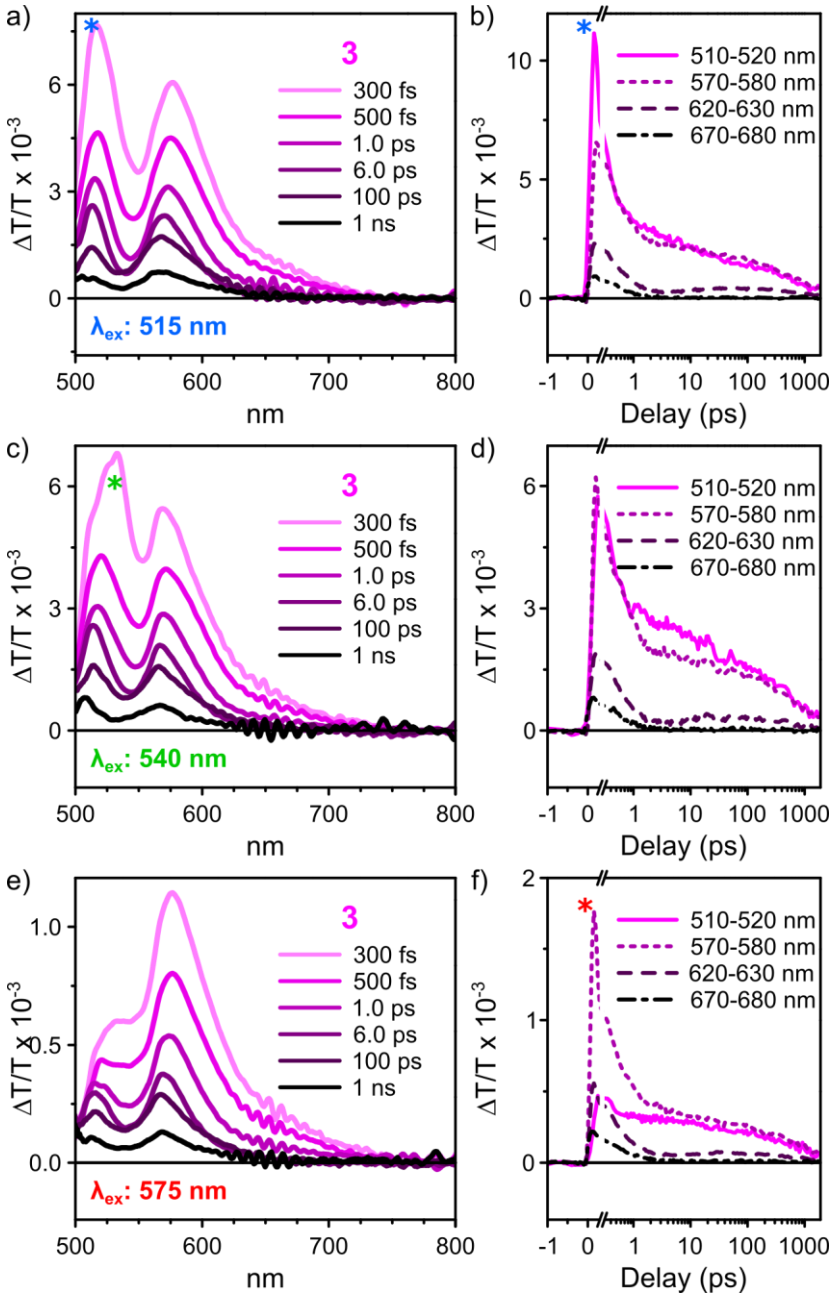

Figure S14. TA excitation dependence of **3**. Spectra (left) and corresponding integrated decay kinetics (right) following excitation at (a, b) 515 nm, (c, d) 540 nm and (e, f) 575 nm Spectra are reproduced from main-text Figure 4. Changing excitation wavelength alters the initial balance between **1**-type and **2**-type excitation but does not significantly change the underlying photophysics (kinetics). Slight distortions induced by pump laser scatter are marked with *.

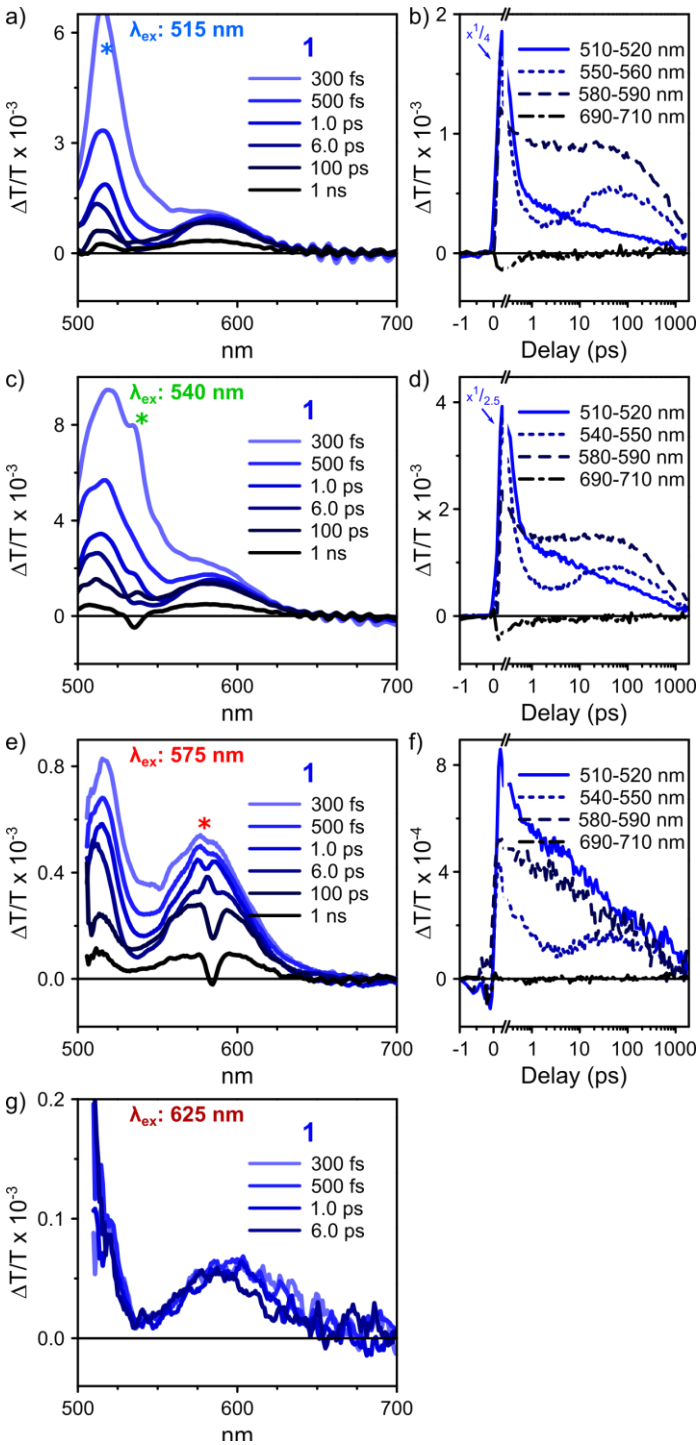

Figure S15. TA excitation dependence of **1**. Spectra (left) and corresponding integrated decay kinetics (right) following excitation at (a, b) 515 nm, (c, d) 540 nm, (e, f) 575 nm and (g) 625 nm. The progressively smaller ΔT/T scale for excitation at 575 nm and 625 nm is a result of the extremely low absorption cross-section in this spectral region. The initial state increasingly resembles species II as the pump photon energy is reduced. Slight distortions induced by pump laser scatter are marked with *.

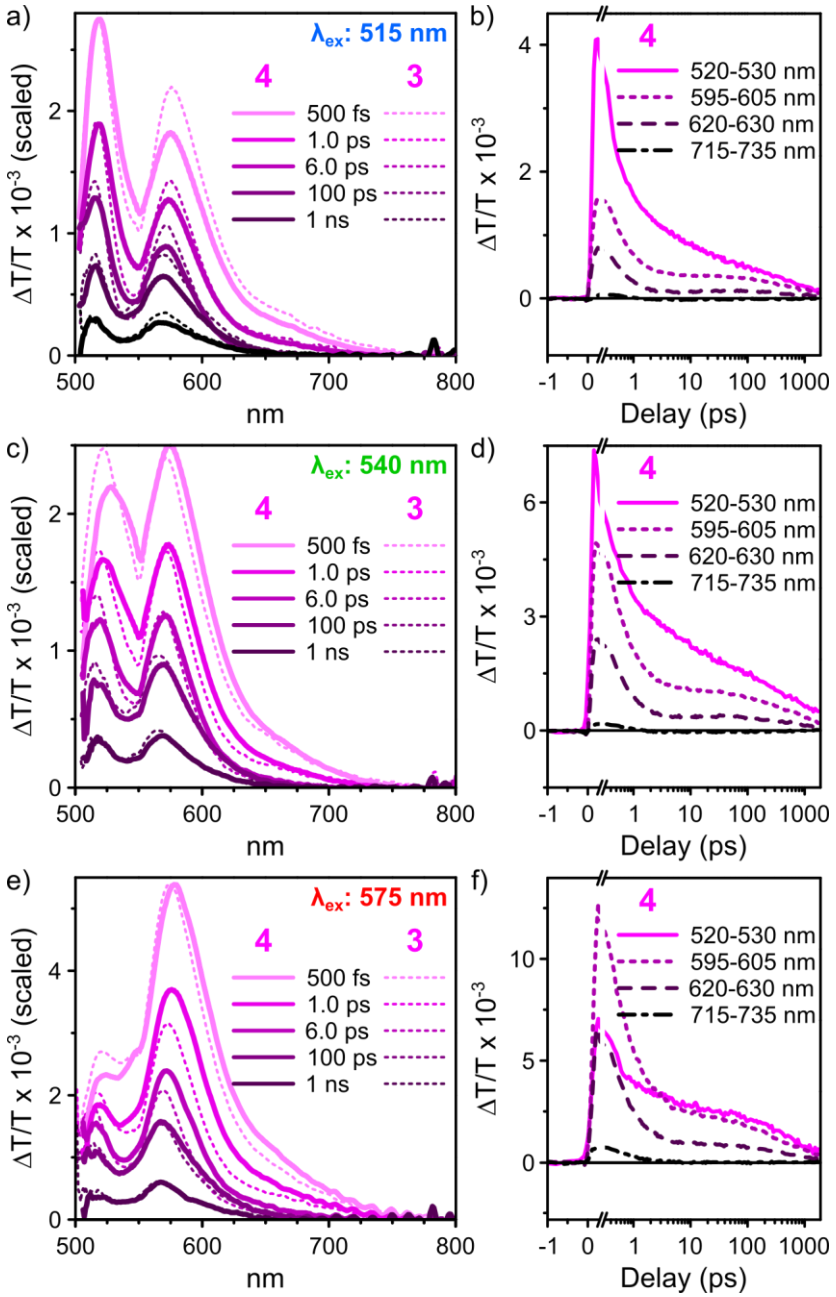

Figure S16. TA excitation dependence of **4**. Spectra (left) comparing **4** (solid) with **3** (dashed) and corresponding integrated decay kinetics (right) following excitation at (a, b) 515 nm, (c, d) 540 nm and (e, f) 575 nm. **4** exhibits less **2**-type signal following excitation at 515 nm and less **1**-type signal following excitation at 575 nm than does **3**, indicating that the delocalization effect described in the main text is slightly weaker in this cage. Nonetheless a similar progression of excited states is observed, suggesting the same underlying processes (I→II→III) are active.

S9. Characterization of host-guest complexes

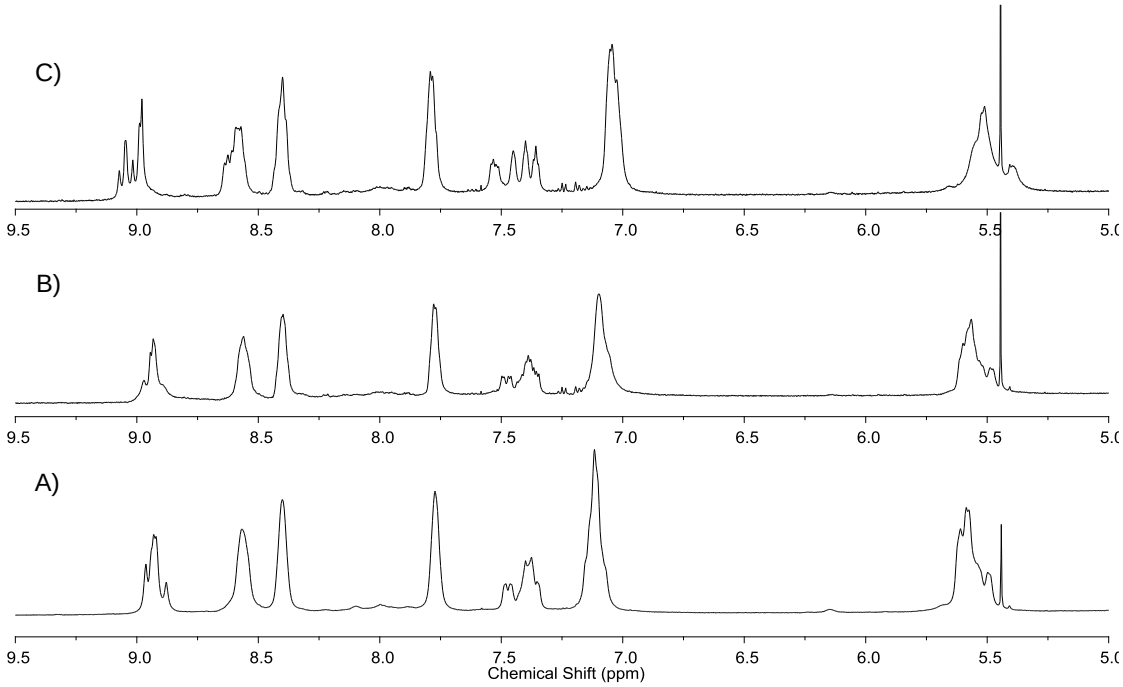

Figure S17. ^{1}H NMR spectrum of (A) cage **1** in the presence of (B) C_{60} and (C) C_{70} in CD_3CN.

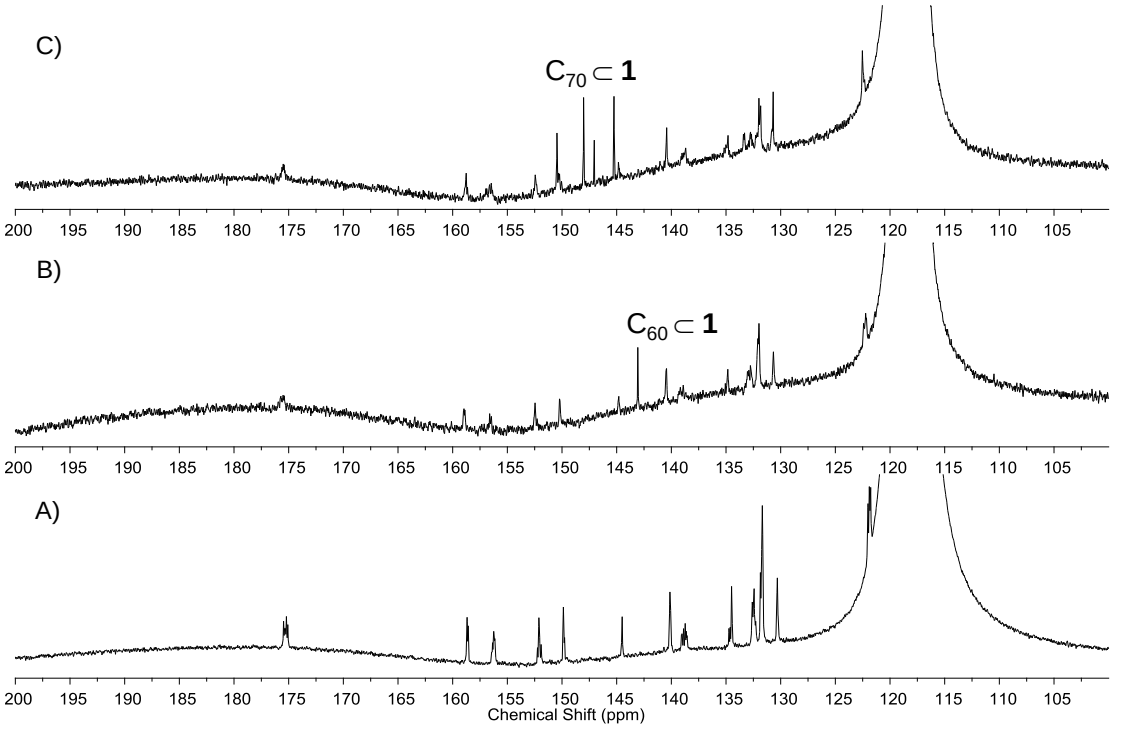

Figure S18. ^{13}C NMR spectrum of (A) cage **1** in the presence of (B) C_{60} and (C) C_{70} in CD_3CN.

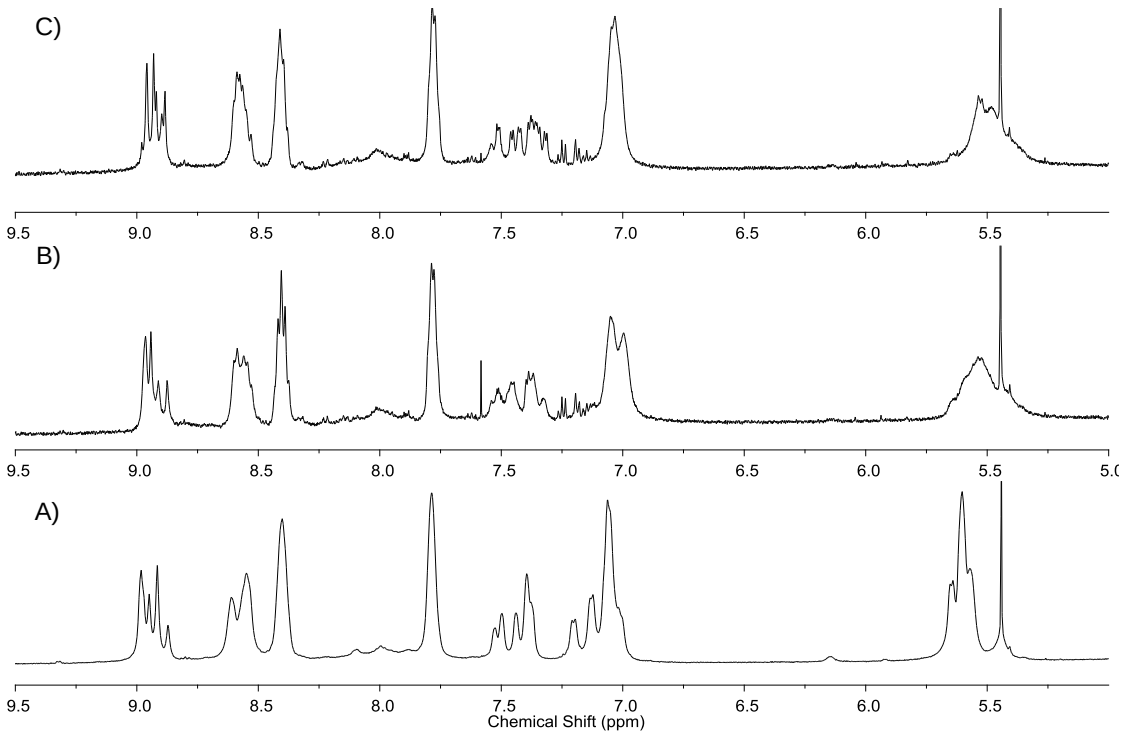

Figure S19. ^{1}H NMR spectrum of (A) cage **2** in the presence of (B) C_{60} and (C) C_{70} in CD_3CN.

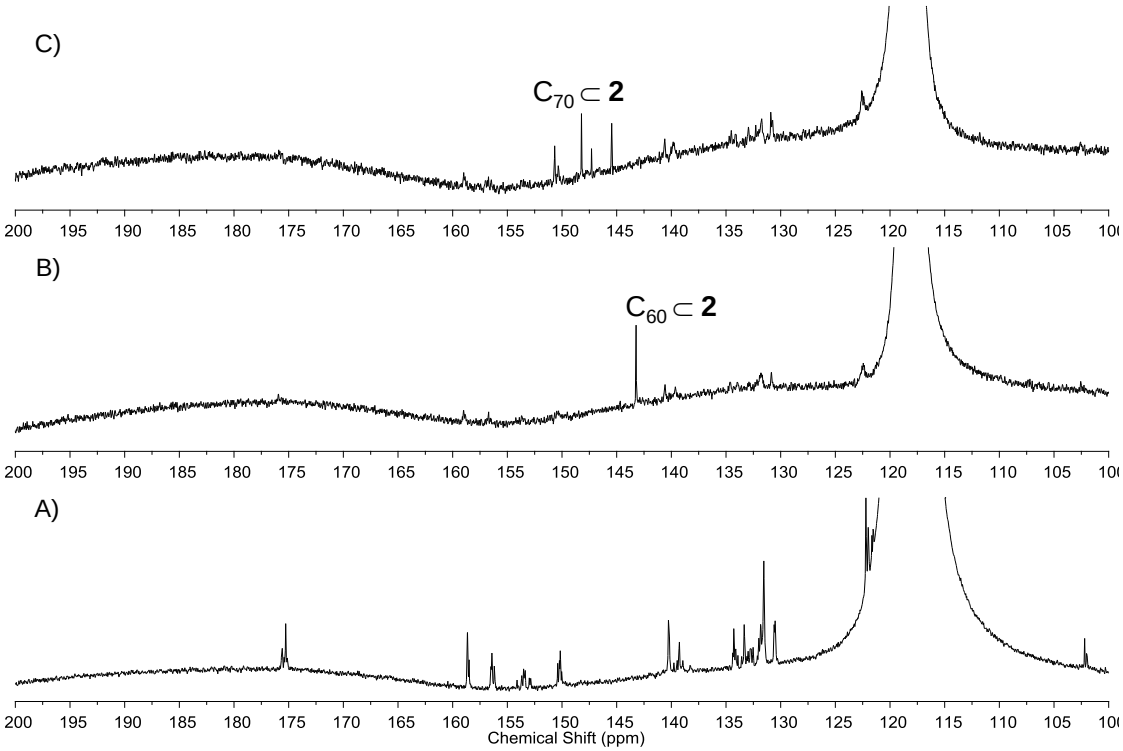

Figure S20. ^{13}C NMR spectrum of (A) cage **2** in the presence of (B) C_{60} and (C) C_{70} in CD_3CN.

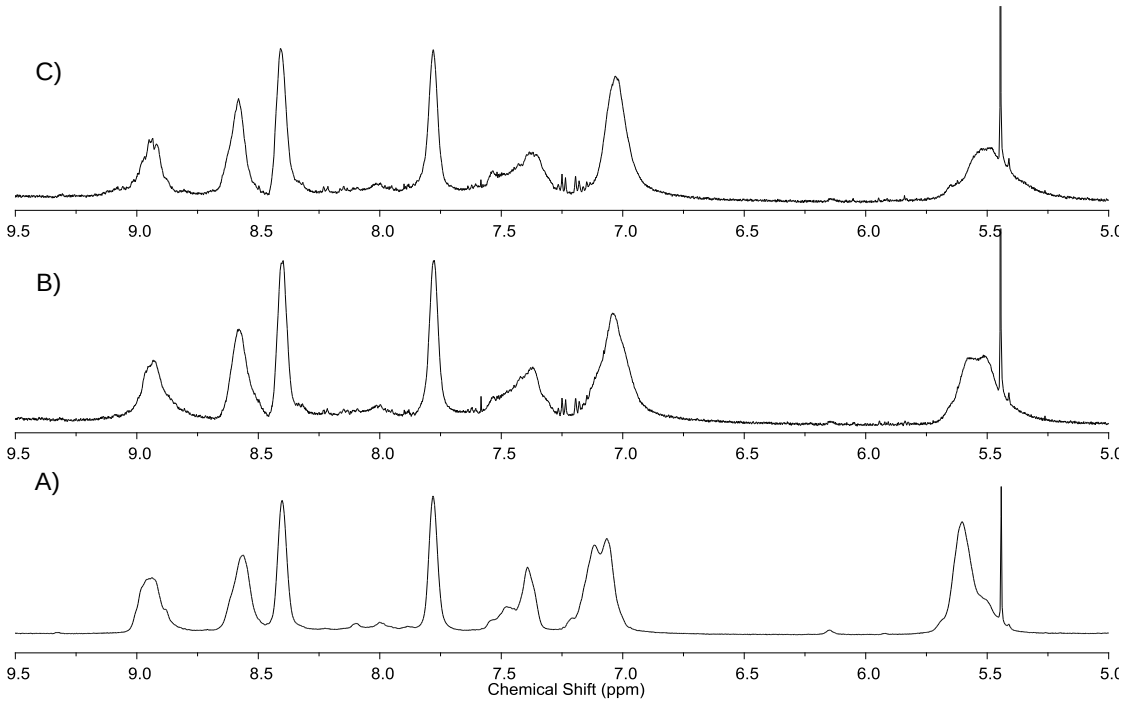

Figure S21. ^{1}H NMR spectrum of collection of (A) cages **3** in the presence of (B) C_{60} and (C) C_{70} in CD_3CN.

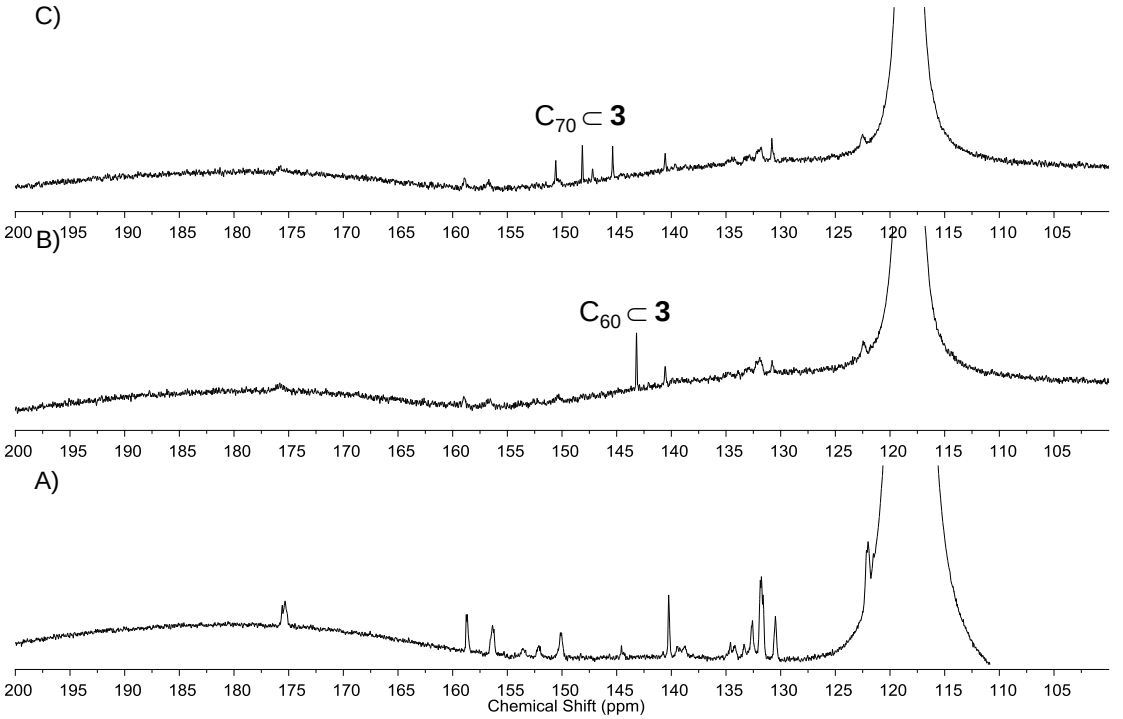

Figure S22. ^{13}C NMR spectrum of collection of (A) cages **3** in the presence of (B) C_{60} and (C) C_{70} in CD_3CN.

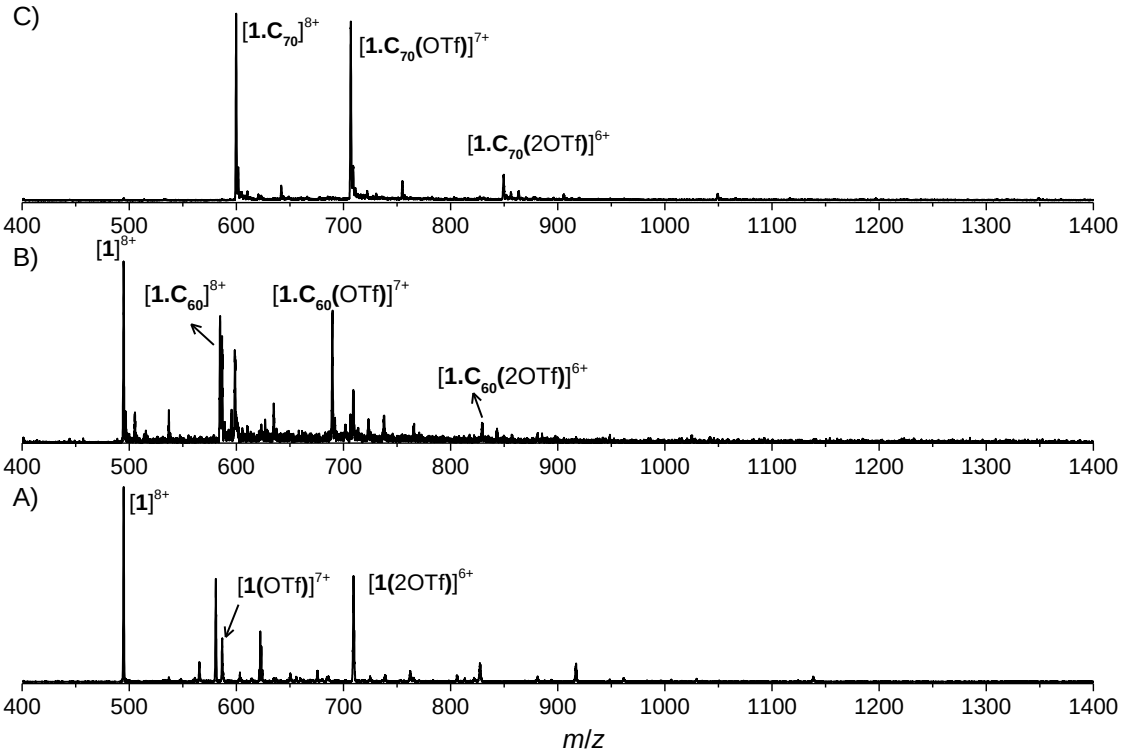

Figure S23. Mass spectrum of (A) cage **1** in the presence of (B) C_{60} and (C) C_{70}.

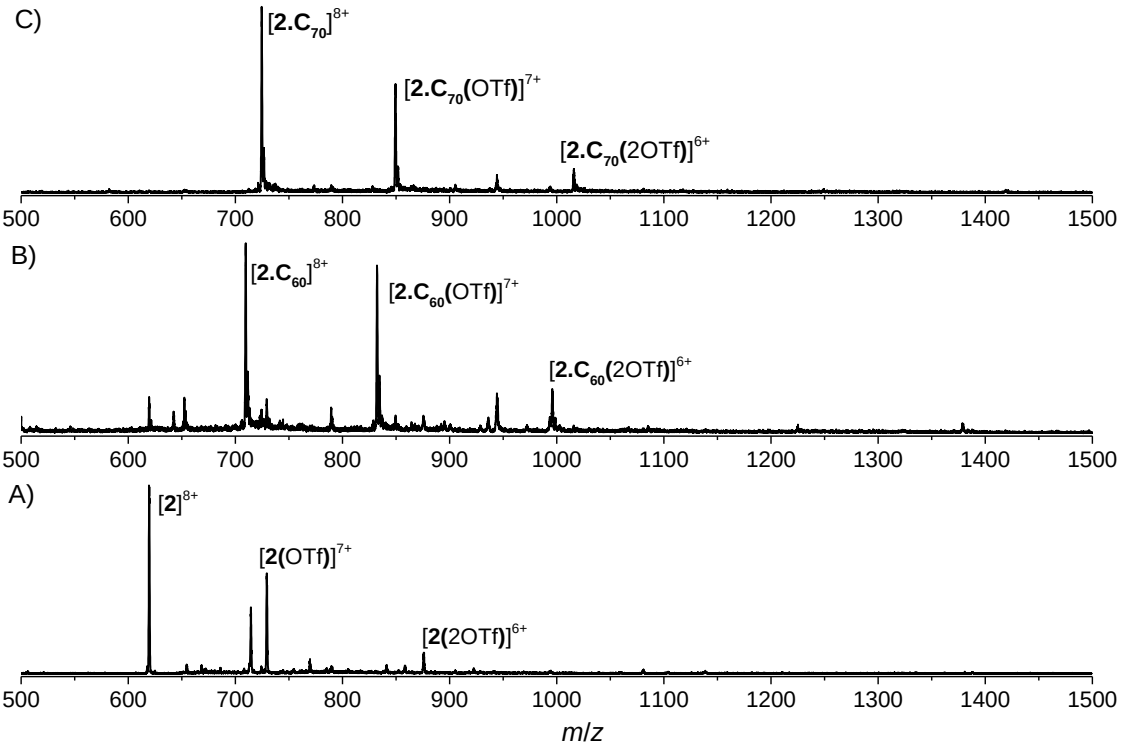

Figure S24. Mass spectrum of (A) cage **2** in the presence of (B) C_{60} and (C) C_{70}.

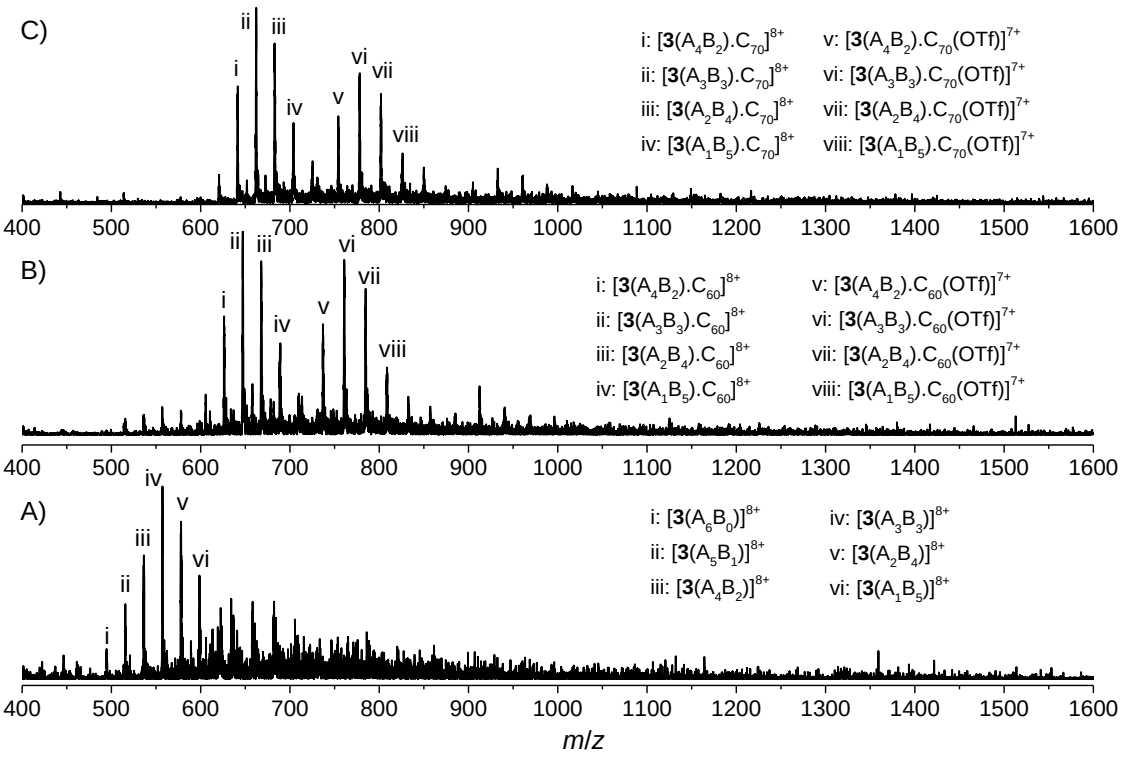

Figure S25. Mass spectrum of collection of (A) cages **3** in the presence of (B) C_{60} and (C) C_{70}.

S10. Fullerene-loaded cage excitation wavelength dependence

Full TA measurements were performed on **1**-**3** encapsulating C_{60} and C_{70} at excitation wavelengths of 515 nm, 540 nm and 575 nm. As discussed in the main text, the signal associated with host-guest charge transfer (new PIA appearing >600 nm) becomes progressively weaker as the pump photon energy is decreased, following the same trend as the excitonic signature (species I) in empty cages. The charge-transfer signal is stronger in the presence of C_{60} than C_{70}, and results in a longer timescale for ground state recovery. In all cages, the spectral evolution and dynamics appear to be consistent with the 'parallel' pathway presented in main-text Figure 6, suggesting that all samples of this type consist of a mixture of fullerene-loaded and empty cages.

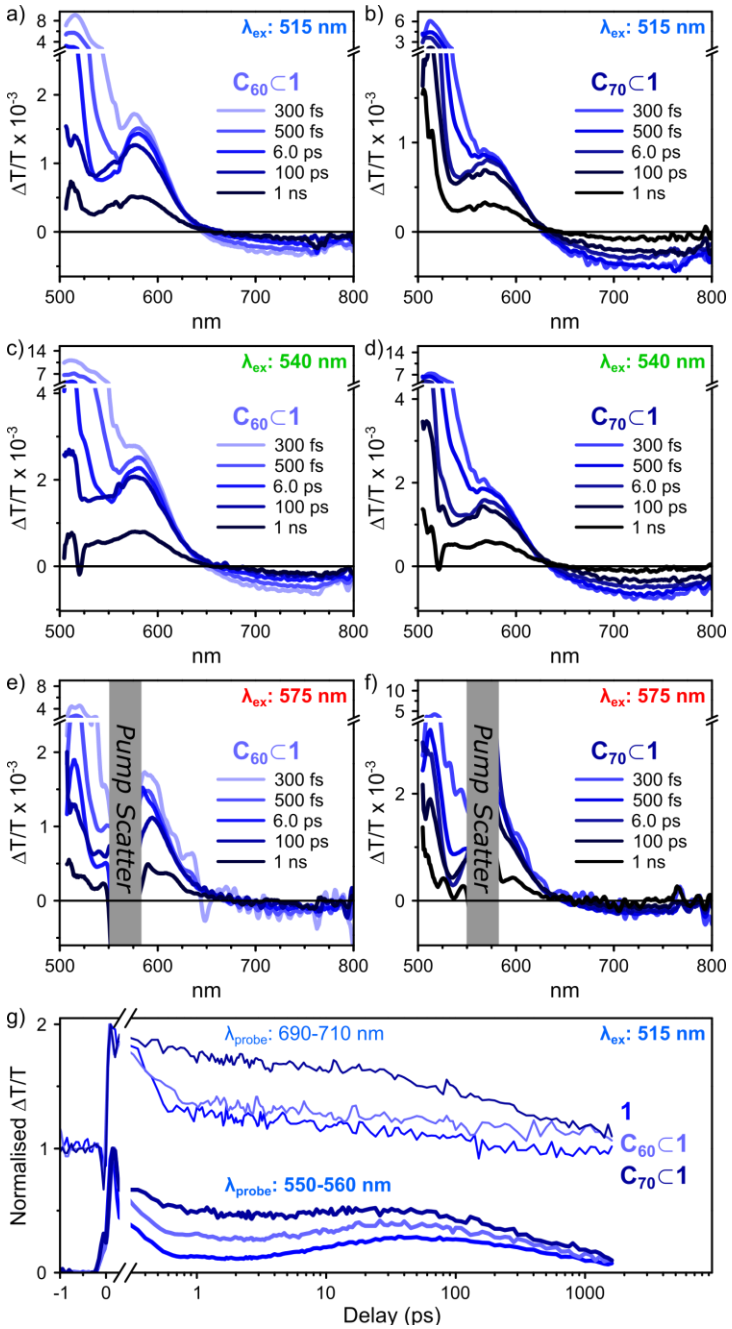

Figure S26. TA excitation dependence of (a, c, e) $C_{60}\subset$**1** and (b, d, f) $C_{70}\subset$**1**, following excitation at (a, b) 515 nm, (c, d) 540 nm and (e, f) 575 nm. The overall spectral shape resembles that of empty **1**, with an additional PIA at long wavelengths attributed to host-guest charge transfer. The relative strength of the charge-transfer signal decreases as pump photon energy decreases. (g) Integrated decay kinetics reveal enhancement of the lifetime and suppression of some of the intrinsic **1** dynamics, especially pronounced in $C_{70}\subset$**1**. Very strong distortions due to pump laser scatter have been removed from the data.

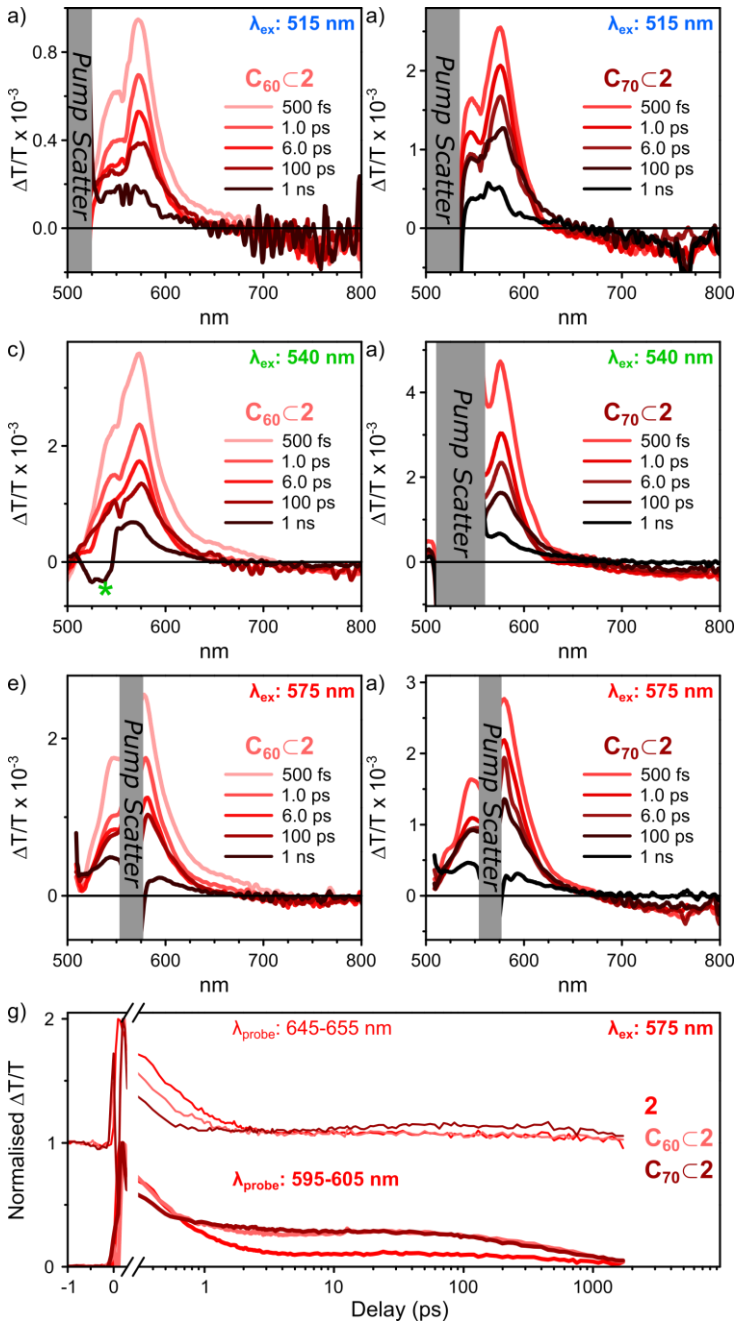

Figure S27. TA excitation dependence of (a,c,e) C_{60}⊂**2** and (b,d,f) C_{70}⊂**2**, following excitation at (a,b) 515 nm, (c,d) 540 nm and (e,f) 575 nm. The overall spectral shape resembles that of empty **2**, with an additional PIA at long wavelengths attributed to host-guest charge transfer. The relative strength of the charge-transfer signal decreases as pump photon energy decreases, though the dependence is much weaker than in fullerene-loaded **1**. (g) Integrated decay kinetics reveal enhancement of the lifetime and suppression of some of the intrinsic **2** dynamics, especially pronounced in C_{70}⊂**2**. Very strong distortions due to pump laser scatter have been removed from the data. Minor distortions are indicated by *.

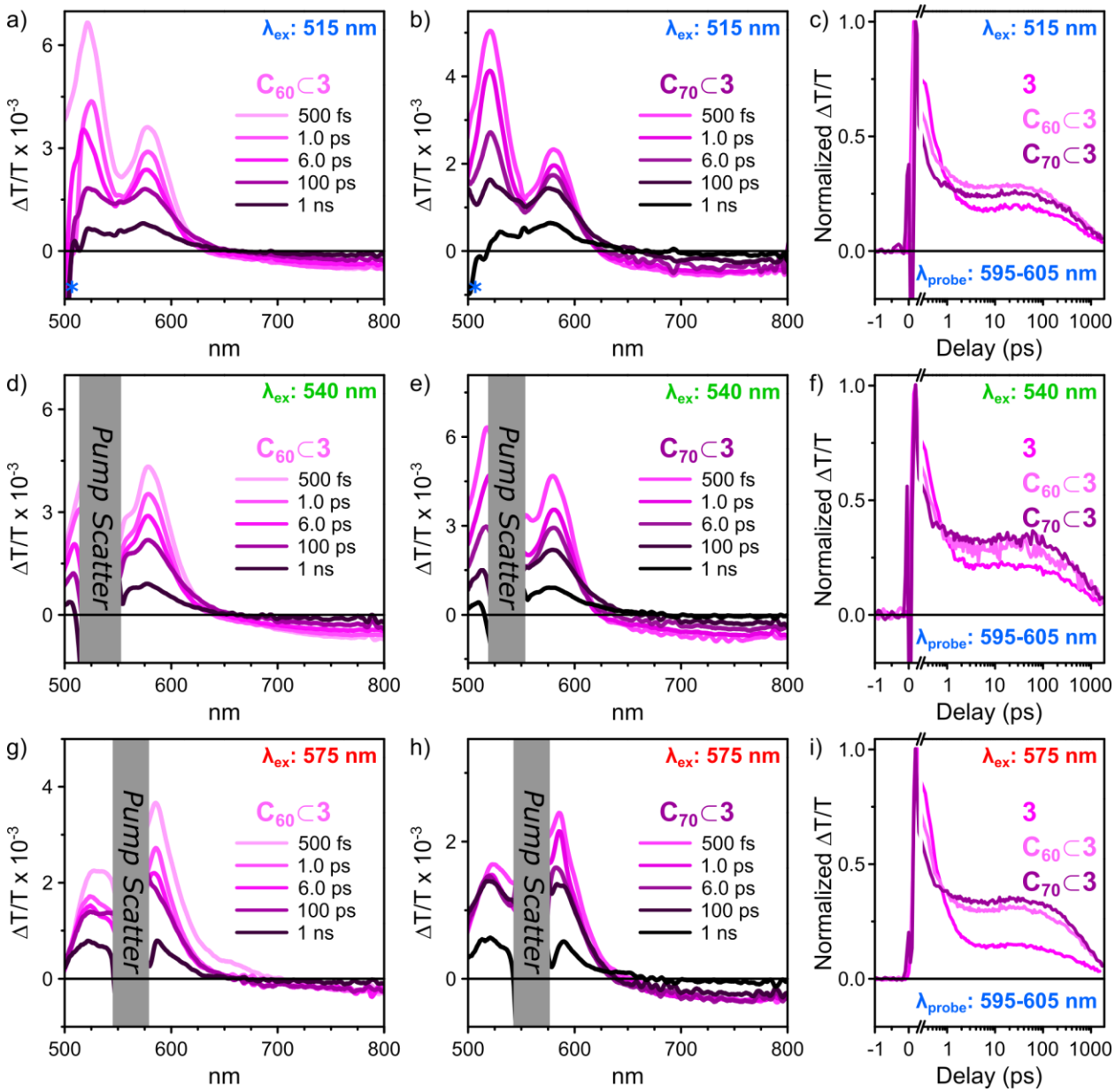

Figure S28. TA excitation dependence of (a, d, g) C_{60}⊂**3** and (b, e, h) C_{70}⊂**3**, following excitation at (a, b) 515 nm, (d, e) 540 nm and (g, h) 575 nm, and (c, f, i) corresponding integrated decay kinetics. The overall spectral shape resembles that of empty **3**, with an additional PIA at long wavelengths attributed to host-guest charge transfer. The relative strength of the charge-transfer signal decreases as pump photon energy decreases. The decay kinetics at all pump wavelengths reveal enhancement of the lifetime and suppression of some of the intrinsic **3** dynamics, especially pronounced in C_{70}⊂**3**. Strong distortions due to pump laser scatter have been removed from the data. Minor distortions are indicated by *.

S11. References

(1) Durantini, A. M.; Greene, L. E.; Lincoln, R.; Martínez, S. R.; Cosa, G. *J. Am. Chem. Soc.* **2016**, *138*, 1215-1225.